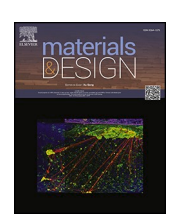
ELSEVIER

Contents lists available at ScienceDirect

Materials & Design

journal homepage: www.elsevier.com/locate/matdes



Design of hot-tearing resistant and thermally stable aluminium alloys for advanced casting technologies

Chengbo Zhu^a, Da Guo^{b,c}, Chu Lun Alex Leung^{b,c}, Iakovos Tzanakis^d, Peter D. Lee^{b,c}, Dmitry Eskin^{a,*}

- ^a Brunel Centre for Advanced Solidification Technology (BCAST), Brunel University of London, UB8 3PH, UK
- ^b UCL Mechanical Engineering, University College London, WC1E 7JE, UK
- ^c Research Complex at Harwell, Harwell Campus, Didcot OX11 0FA, UK
- ^d School of Engineering, Computing and Mathematics, Oxford Brookes University, Oxford OX3 0BP, UK

ARTICLE INFO

Keywords: Aluminium alloys Alloy design Solidification contraction Thermal stability Low cracking susceptibility

ABSTRACT

Aluminium alloys are cost-effective and lightweight materials that are widely used in the transport industry, where cost and weight are key considerations for material selection. Operating at elevated temperatures (T \geq 0.5T_m, where T_m is the absolute melting temperature of Al) is known to be a weakness of these alloys. A new methodology is proposed to design Al alloys with improved thermal stability and reduced cracking susceptibility using both theoretical and experimental techniques. In this work, two new alloys based on the Al-Ce-Fe-Mn-Ni system were developed. To minimise hot tearing, compositions with a narrow freezing range during the final stage of solidification were selected. Thermal contraction upon solidification was then experimentally determined as a measure of hot tearing susceptibility, and compositions with low thermal strain accumulation were identified. Following exhaustive screening, the solidification behaviour was further investigated by examining the microstructural morphologies under different cooling rates, followed by mechanical testing. Results showed that a high proportion of the strength (75 to 80 %) was retained after tensile testing at 300 °C. The methodology can be applied to designing Al alloys for both casting and additive manufacturing applications.

1. Introduction

Aluminium alloys are extensively used in a wide range of applications where high strength and low density are desired properties to improve energy efficiency and reduce carbon footprint, such as in the transportation and aerospace industries [1–3]. There has been constant demand for new alloys that are lighter, stronger, and more heat-resistant

The most used Al casting alloys are based on the Al-Si-(Mg, Cu) system due to the low cracking susceptibility and good castability, in addition to the adequate mechanical and corrosion properties [4]. Hot tearing, being one of the major concerns for developing new Al alloys, is an inherent problem for Al alloys due to their large solidification shrinkage and thermal contraction. It is mainly caused by a lack of liquid feeding between dendrites at the final stage of the solidification [5]. The addition of Si in the Al alloys lowers the cracking tendency by increasing the amount of eutectics and decreasing the solidification shrinkage and contraction [6].

During solidification, the alloy reaches coherency temperature when the grains in the liquid impinge and form a continuous network. Below the coherency temperature, the network starts to become rigid (rigidity point), and thermal stresses subsequently accumulate due to solidification shrinkage and thermal contraction while being compensated by liquid feeding. The liquid feeding becomes restricted with increasing solid fraction, leading to a reduced permeability of the solid network for the liquid to flow through. When the stresses and strains cannot be accommodated by the semi-solid network, hot rearing occurs [7]. The key is to keep the liquid feeding adequate. A small freezing range promotes good liquid feeding and thus a low cracking susceptibility. The Scheil solidification path calculation can be used for the design of alloys with a nonequilibrium solidification range, typically for those that are close to the eutectic compositions. The cracking susceptibility in those alloys is lower because the liquid feeding due to the sufficient amount of low-melting eutectics is adequate to compensate for the solidification shrinkage [7]. The hot tearing occurs in an "effective" or "vulnerable" solidification range, i.e. the temperature range between the coherency

E-mail address: dmitry.eskin@brunel.ac.uk (D. Eskin).

^{*} Corresponding author.

point and the solidus (equilibrium or nonequilibrium). Above the coherency point, the grains move freely in the liquid, and the alloy cannot retain its shape. The contraction is only detectable when the rigid skeleton develops. It was identified that the critical range of solid fraction for hot tearing to happen is from 0.90 to 0.99 [7,8], before the very end of solidification where a strong solid network becomes able to endure the accumulated stresses and imposed thermal strains [9]. The contraction in the effective solidification range, also known as linear solidification contraction, can be used as an indicator of cracking susceptibility [8], and it can be evaluated experimentally [10,11]. The cracking susceptibility is lower if the compositions have narrow freezing ranges and small thermal contraction.

In commercial Al-Si-(Mg, Cu, Ni, Fe) alloys, the Si addition also improves the strength by forming a reinforcing network of Si and intermetallic particles in the microstructure [12]. The strength, however, deteriorates at the operating temperature over 200 $^{\circ}\text{C}$ due to the particle coarsening and partial dissolution of the microstructural constituents [13]. To fulfil the demand for using lightweight and cost-effective alloys at elevated temperatures, i.e. temperatures around or higher than 0.5 T_m , where T_m is the melting temperature (in K) of the alloys. It is necessary to design a new category of thermally stable Al alloys, which retain their microstructure and most of their strength at the intended service temperatures.

Intermetallic coarsening, where eutectic grains or intermetallic particles grow at the expense of smaller ones, is mainly controlled by the diffusion of alloying elements and their solubility in the Al matrix. During this process, the solute atoms move through the matrix from finer to larger particles, causing overall coarsening. The movement of solute atoms in the matrix is slower when their diffusivity and solubility are small, thus retarding the coarsening process [14]. In Al alloys, the most used alloying elements that meet the requirement of slow diffusion are mainly of two categories, namely transition metals (TM) and rare earth (RE) elements [15]. They are typically added to improve the stability of the microstructure in Al alloys at elevated temperatures.

Cerium, Ce, is abundant in Earth's crust (about two times the amount of Cu), has drawn attention to the development of thermally stable Al alloys [16]. Al-Ce alloys have the potential to be a base system for hightemperature engineering applications [17,18]. The diffusion rate of Ce in Al is five orders of magnitude lower than Si at 500 °C [19,20]. Its solubility in Al is relatively low [17]. Weiss [21] reports that a cast Al-10 Mg-8Ce (wt%) alloy retained 75 % of the strength (97 MPa) after 336 h of heating at 260 °C, being better than AA2618-T61. The yield strength of the alloy was more than twice that of AA2618-T61 (131 MPa vs 62 MPa) which is an Al-Cu-Mg-Ni-Fe alloy commonly used for pistons and rotating aircraft parts with working temperatures over 200 °C. The excellent thermal stability was attributed to the extremely low solubility of Ce and the stable Ce-containing intermetallics, which prevented grain coarsening. The properties of Al-Ce-Mg alloy may be further strengthened by adding Sc or Zr [22]. Moreover, Ce addition improves melt fluidity and permeability through eutectic formation, resulting in a lower cracking susceptibility [16].

Various manufacturing methods, e.g. conventional casting or additive manufacturing (AM), have been used to study properties at elevated temperatures for several ternary Al-Ce-TM systems, such as Al-Ce-Cu [23], Al-Ce-Fe [24], Al-Ce-Ni [25,26], and Al-Ce-Mn [27,28]. Those alloys showed promising thermal stability for high-temperature applications because of the stable intermetallic phases formed in the microstructure and/or the low solubility/diffusivity of the alloying elements that resist structure coarsening. High-temperature properties were also investigated in Al-Ce-TM alloys with more than one TMs [29–33]. However, the comprehensive alloy design that combines low hot-tearing susceptibility and thermal stability has not been done yet, although the combination of these properties is crucial for a wide range of applications, from automotive to electronic and aerospace; as well as for manufacturing these alloys through a variety of technologies, from die casting to additive manufacturing.

Here, we propose a methodology for searching thermally stable compositions with low cracking tendency. The first step is to select alloying elements. Two criteria should be considered: low diffusivity in pure Al and the formation of intermetallics with Al near the melting point of Al (above 600 °C). Generally, transition metals or rare-earth elements meet the criteria. The selection of alloving elements is followed by the search for compositions close to the eutectic to minimise the freezing range. After the freezing ranges of the selected compositions are calculated, e.g. using Thermo-Calc, their solidification contraction is experimentally evaluated. Those compositions with a small freezing range and low solidification contraction are favoured for further characterisation. The alloys can be heat-treatable upon annealing if Zr is added to form stable Al₃Zr dispersoids. For specific applications with preferred microstructures, the microstructural morphologies at various cooling rates were examined by casting in a wedge mould. This methodology can be applied to conventional manufacturing methods, such as casting, and advanced manufacturing, like AM, where rapid cooling often causes hot tearing in Al alloys due to the high thermal gradients, leading to high thermal strain and stress.

In this study, the methodology was applied to the development of two alloys with high thermal stability and low cracking susceptibility. Being a common impurity in Al alloys, Fe was considered here to be the third alloying element in addition to Al and Ce, enabling the potential use of recycled feedstock. Two other low-cost alloying elements, Ni and Mn, which improve the mechanical and thermal properties of Al alloys, were also added.

2. Methods and materials

To cost-effectively select alloy compositions with a narrow freezing range, computer coupling of phase diagrams and thermochemistry (CALPHAD) was employed. Thermo-calc 2024a with TCAl8 database was used in this study [34].

For experimental trials, the alloys were prepared with commercially pure 99.9 % Al, Al-10Ce, Al-10Fe, Al-20Mn, Al-20Ni, and Al-10Zr (wt%) master alloys. 0.7 kg of each alloy was placed in a clay-graphite crucible and melted in an electric resistance furnace at 810 °C. The melt was poured at 760 °C into a wedge mould, which was pre-heated to 150 °C before casting. At different heights in the mould, various cooling rates were achieved during the solidification. The microstructures at three positions, 20 mm, 50 mm, and 80 mm from the top, were characterised for each composition. The range of cooling rate was between 78 °C/s and 0.33 °C/s from the top to the bottom of the mould. The dimensions of the wedge mould and the positions of samples for microstructural characterisations are shown in Fig. 1.

The linear solidification contraction was measured in a device shown in Fig. 2. The setup was similar to the technique introduced in [10,11].

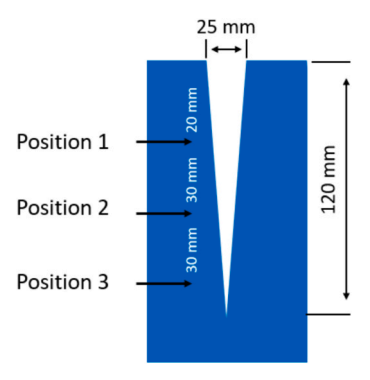


Fig. 1. Dimension and geometry of the wedge mould used in the experiment. The microstructures at the three positions were characterised. The corresponding cooling rates for positions 1 and 3 are 78 $^{\circ}$ C/s and 0.33 $^{\circ}$ C/s, respectively.

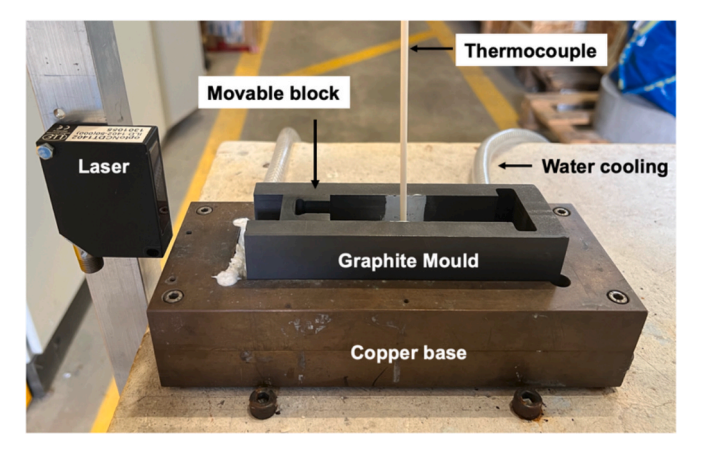


Fig. 2. An experimental setup for measuring the solidification contraction.

On top of a water-cooled copper base was a T-shaped graphite mould (100 mm long and 25 \times 25 mm in cross section) with a moving block near its left end. The moving block also had a T-shaped cavity for the solidified sample to pull toward the other end during cooling. A laser sensor (optoNCDT IDL 1402-50) recorded its travelling distance, which was used to calculate the expansion, shrinkage and contraction of the alloy. A K-type thermocouple was placed in the centre of the graphite mould at 1 mm from its bottom to record the temperature that was then related to the measured displacement. The data were recorded using a National Instruments DAQ with an acquisition rate of 50 Hz. At least three measurements were performed for each alloy.

The phase composition of the cast samples was identified using a Brucker D500 X-Ray Diffractometer (XRD). The measurements were performed using $\text{CuK}\alpha$ radiation with a wavelength of 1.5406 Å. A 20 range of $20{-}90^\circ$ was used with an interval step of 0.02° . The specimens were prepared from the samples produced as a result of the linear solidification contraction measurements. The microstructure and fracture surfaces were analysed using a TESCAN MAGNA Scanning Electron Microscope (SEM) equipped with a backscattered electron (BSE) detector. The elemental distribution was mapped in the SEM equipped with an Oxford ULTIM MAX 65 Energy Dispersive X-ray Spectroscopy (EDS) Detector. Prior to the SEM examination, the samples were cut, ground and polished using the standard techniques. AZtech software was used to process and analyse the mapping data.

The mechanical properties of the two alloys were evaluated by a profilometry-based indentation plastometry (PIP) [35] and tensile test in compliance with ASTM standard E8/E8M-24 [36]. In the PIP test, an indenter made of WC-Co cermet of a radius of 1 mm was pushed into the sample with a known force, followed by a mapping of the indent profile. An iterative finite element analysis (FEM) embedded into the PIP software [35] was performed to fit the indent profile. When a best-fit set of plasticity parameter values was obtained, it led to the true stress-strain relationship. Note that the tensile properties are estimated based on a constitutive model in software [35]. As the real experiment is done under compressive conditions, the tensile properties show the potential properties of a defect-free sample while the elongation is defined as a uniform deformation (prior to necking in tensile tests). The PIP test was conducted under two conditions: room temperature and at 300 °C after holding for 10 min at this temperature. Two tests were carried out for each condition. Uniaxial tensile tests were conducted on as-cast cylindrical samples. The length of the reduced section was 30 mm, with 5 mm diameter. Testing was performed on an Instron 5892 tensile tester. Two conditions were tested: room temperature and 300 °C after 10 min of heating. Three tests were carried out for each condition.

3. Results

3.1. Composition selection using CALPHAD

Fe is known to be an inevitable impurity in Al. It can also contribute to the alloy's strength if its concentration is carefully selected [37]. It is better to utilise Fe as an alloying element reinforcing the microstructure rather than trying to reduce its amount by using ever purer feedstock. A minor content of Fe, 0.3 wt%, was, therefore, added to the alloy. Ce was selected because it improves melt fluidity and permeability through eutectic formation while forming phases that resist grain coarsening at elevated temperatures [16-18]. Mn and Ni were considered as the additional alloying elements because they possess the potential to improve the strength in an Al-RE system [25,28]. Designing aluminium alloys for applications used above 300 °C remains challenging. There is still a knowledge gap, despite previous works to search for alloys that can work at elevated temperatures. When selecting alloying elements and designing alloys, the requirements of targeted applications need to be defined. Other TMs may also improve the properties or even be more suitable for particular applications. However, to systematically select alloying elements and develop alloys for those purposes, further research is required to bridge the knowledge gap on how the TMs and RE elements influence the microstructures and properties in unconventional aluminium alloys.

In this work, the design was based on Al-Ce-0.3Fe-Mn-Ni system. The eutectic composition in the Al-Ce binary system is near 12 wt% Ce. The Al alloys with Ce concentrations from 8 wt% to 12 wt% have been studied substantially and those alloys showed promising thermal stability for high-temperature applications. Ce concentrations below 8 wt% were explored in this work to achieve a lower density in the Al alloy while maintaining thermal stability and lower cracking susceptibility. The Scheil equations for three different Ce concentrations, 4.0, 6.0, and 8.0 wt%, are shown in Fig. 3(a), (b), and (c), respectively. Al₃₁Mn₆Ni₂, Al₄Mn, Al₆Mn, and Al₁₂Mn phases were restricted in the calculations as they were not experimentally observed in similar alloy systems [32,38,39]. The Mn and Ni concentrations were determined according to the eutectic composition of the corresponding alloys. They are Al-4Ce-0.3Fe-1.43Mn-3.85Ni, Al-6Ce-0.3Fe-1.12Mn-2.88Ni, and Al-8Ce-0.3Fe-0.89Mn-2Ni. The freezing ranges of eutectic reactions for all three alloys were relatively low, less than 3.7 $^{\circ}$ C. In terms of phases formed by the end of solidification, the difference between these alloys was in the formation of Al₁₃Fe₄, which is hard and brittle. It formed in the alloys with 6 wt% and 8 wt% Ce. Stresses can easily be concentrated on the tips of the needle-shaped and flake-shaped Al₁₃Fe₄, resulting in crack nucleation and low ductility [40]. To avoid Al₁₃Fe₄, Ce concentration below 6 wt% was considered. In the range of 4 wt% and 6 wt%, it was found that the alloy Al-4.6Ce-0.3Fe-1.3Mn-3.77Ni had the lowest freezing range of 1.12 °C, as shown in Supplementary Materials (Fig. S1 and Table S1). The volume fraction of the solidification in the third step was over 96 % (the third stage of solidification in Fig. 3d). This gives better control of the phase formation upon the solidification, even in rapid cooling, as the four intermetallic phases form simultaneously.

With increasing cooling rate, the eutectic equilibria frequently shift, making hypereutectic alloys closer to the eutectic or even hypoeutectic alloys in structure. With this in mind, we investigated the phase formation of hypereutectic alloys of Al-4.6Ce-0.3Fe-Mn-Ni system. The projection of the liquidus surface is presented in Fig. 4. The liquidus surface is for the equilibrium conditions, which may be different from the solidification conditions in the Scheil approximation, although the liquidus temperature is typically not much affected by the cooling rate. For hypereutectic compositions in the alloy system, the possible primary phases are Al₈M₄Ce (M represents Fe, Mn, or/and Ni), Al₂₃Ni₆Ce₄, or Al₃Ni, depending on Mn and Ni concentrations. As can be seen, Al₈M₄Ce is stabilised with the increasing Mn concentration while the increase in Ni promotes primary phase Al₃Ni first, and Al₂₃Ni₆Ce₄ upon further addition.

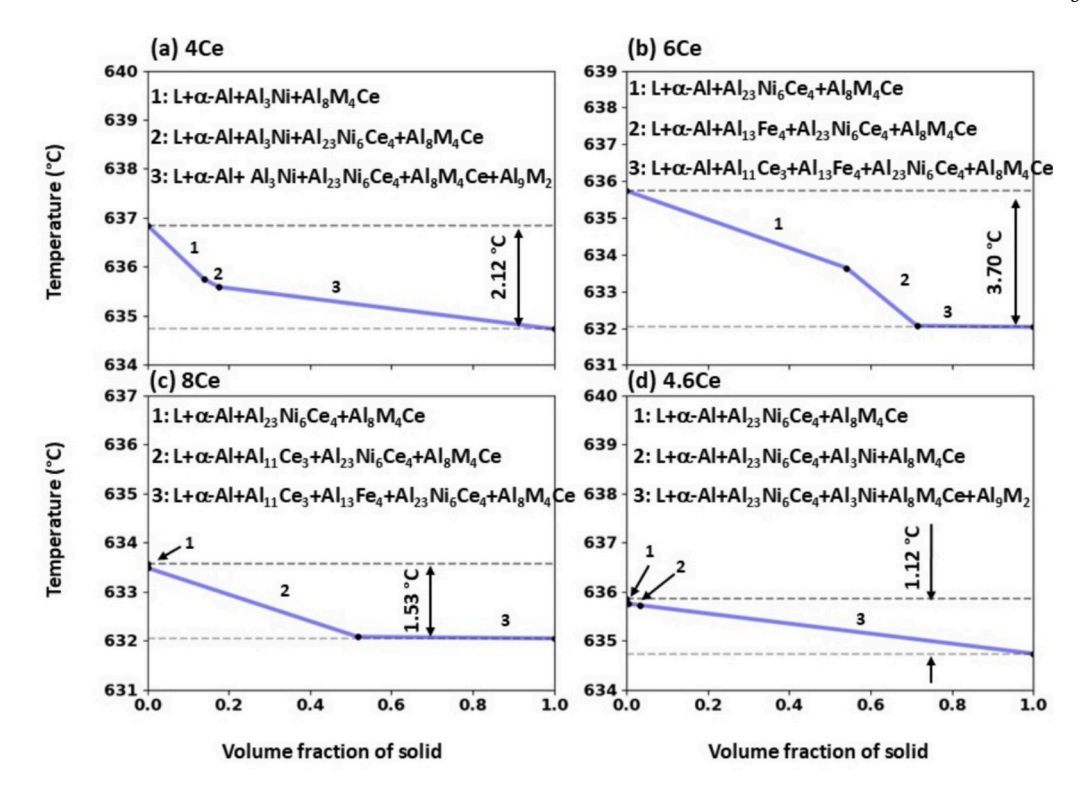


Fig. 3. Scheil solidification paths of the near eutectic alloys based on Al-Ce-0.3Fe-Mn-Ni system with (a) 4.0Ce, (b) 6.0Ce, (c) 8.0Ce, and (d) 4.6Ce, respectively; the concentrations of Mn and Ni were determined from the eutectic compositions. The compositions are (a) Al-4Ce-0.3Fe-1.43Mn-3.85Ni, (b) Al-6Ce-0.3Fe-1.12Mn-2.88Ni, (c) Al-8Ce-0.3Fe-0.89Mn-2Ni, and (d) Al-4.6Ce-0.3Fe-1.3Mn-3.77Ni, respectively.

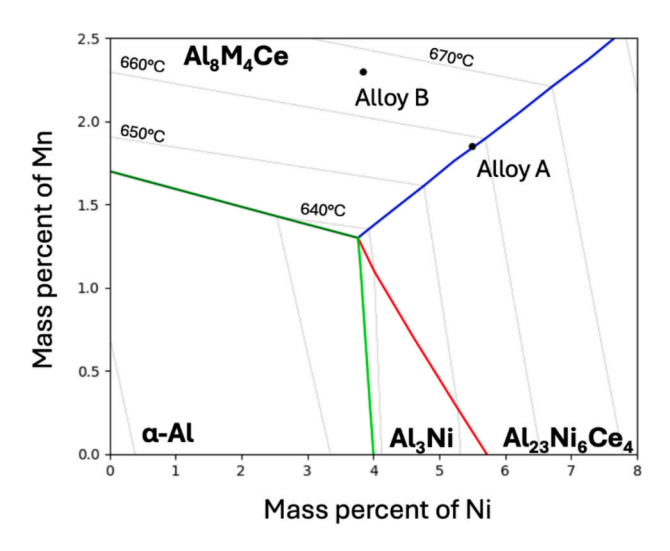


Fig. 4. The liquidus projection of the Al-4.6Ce-0.3Fe-Mn-Ni system. The isotherms (grey lines) indicate the temperatures at an increment of 10 $^\circ\text{C}.$

The first selected composition (Alloy A) was Al-4.6Ce-0.3Fe-1.84Mn-5.5Ni, which sits in the valley between $\rm Al_8M_4Ce$ and $\rm Al_{23}Ni_6Ce_4$. Hence, there were two types of intermetallic forming at the beginning of the solidification. The other composition (Alloy B) was Al-4.6Ce-0.3Fe-2.3Mn-3.84Ni, whose solidification path in equilibrium condition (after formation of the primary $\rm Al_8Mn_4Ce$ phase) goes straight to the eutectic point near 1.84Mn-5.5Ni. The Scheil curves of the two alloys are shown in Fig. 5(a) and (b), respectively. The volume fraction of intermetallics for Alloy A and Alloy B is 14.7 vol% and 12.41 vol%, respectively. It is noteworthy that the increase in Mn concentration and decrease in Ni concentration make the cost of the alloys potentially lower.

3.2. Experimental results

The BSE images for each alloy at three different positions in the wedge mould are shown in Fig. 6. The microstructure became finer as the position changed from position 1 to position 3, i.e. with the increase in cooling rate.

As can be seen from Fig. 6(a) and Fig. 6(b), the bright coarse faceted particles and plate-like grey intermetallics in Alloy A were surrounded by eutectic colonies. In Fig. 6(d), the microstructure was considerably finer, with the largest particles at the scale of about 10 μ m. Primary faceted particles were not observed anymore, suggesting a shift in the equilibrium towards eutectic solidification. Two distinctive contrasts were observed in eutectic areas: grey and bright.

In Alloy B (Fig. 6e), slower cooling led to a microstructure consisting of a mixture of fine eutectic colonies (bright areas) and the needle-like grey intermetallics between them, with dispersed bright particles. With increasing cooling rate (Fig. 6f), the needle-like grey phases became much finer, forming a typical eutectic structure. The dispersed bright particles became finer. In Fig. 6(g), the microstructure was further refined with a higher cooling rate. More distinct areas of the Al solid solution dendrites appeared while bright particles were not observed anymore, suggesting a shift of the equilibrium towards hypoeutectic solidification.

The XRD patterns of Alloy A and Alloy B of slow cooling (at position 1) presented in Fig. 7 helped decipher the phase composition and the nature of the particles observed in Fig. 6. The selection of phases was the same in both alloys. They are $\alpha\text{-Al},\ Al_9M_2$ (M represents Ni and Fe), $Al_{23}Ni_6Ce_4$, and $Al_{20}Mn_2Ce$. Significant presence of peaks corresponding to phases Al_9M_2 (blue circles) and $Al_{23}Ni_6Ce_4$ (green triangles) indicated their widespread formation within the microstructure.

EDS map analysis of Alloy A and Alloy B after slow cooling (position 1) and fast cooling (position 3) is shown in Fig. 8. At position 1, the eutectic phases in Alloy A consisted mainly of Ni, Ce, Mn, and Fe. A similar elemental distribution was also found in the large bright particle.

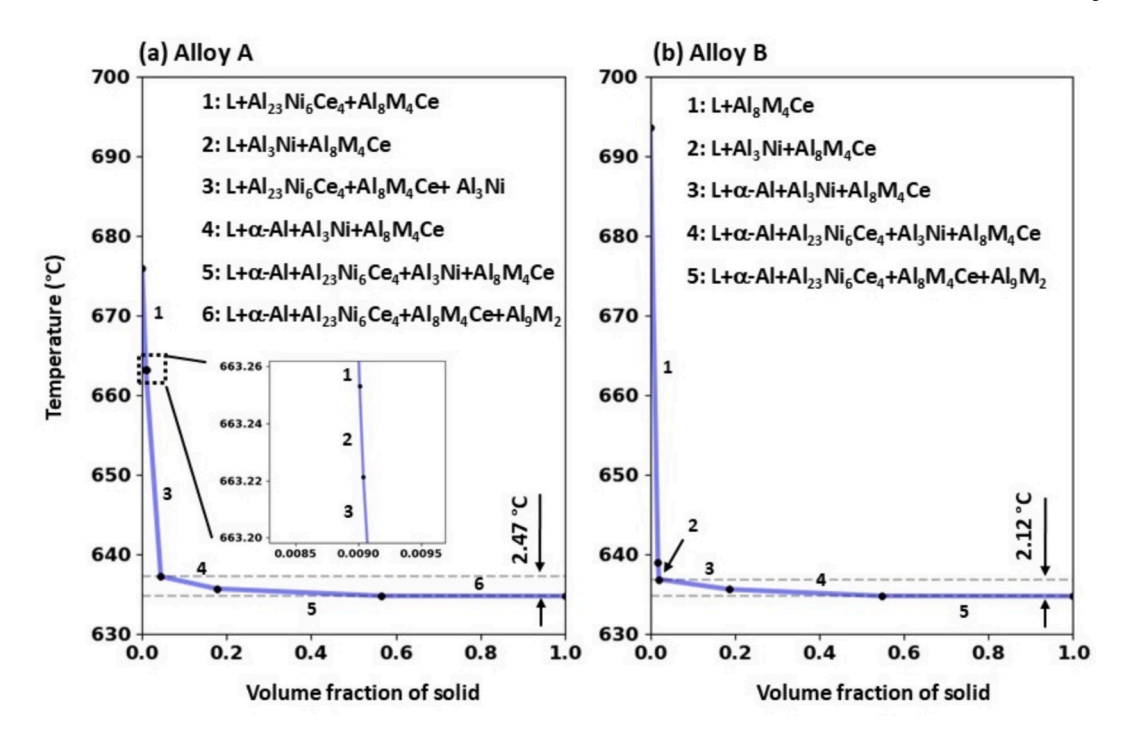


Fig. 5. Solidification paths of (a) Al-4.6Ce-0.3Fe-1.84Mn-5.5Ni and (b) Al-4.6Ce-0.3Fe-2.3Mn-3.84Ni alloys calculated using the Scheil approximation.

Ni, Fe, and Mn were observed in the plate-like intermetallics, while the black areas in the BSE image showed a high concentration of Al. With fast cooling (position 3), the two distinctive areas in the eutectic phases (grey and bright) observed in the BSE image contained different element distributions: the grey eutectic area showed a strong contrast of Ni and Fe, while the bright eutectic area showed a strong contrast of Ni and Ce. The globular particles contained Mn and Ce.

In Alloy B, the microstructure formed under slow cooling showed a high contrast of Ni, Ce, and Fe in the fine eutectic phases. The needle-like grey particles contained Ni, Fe, and Mn. The dispersed bright particles consisted of Mn, Ce, and Fe. Faster cooling at position 3 in the alloy produced dispersed bright particles with similar elemental distributions to those at position 1, but at a finer scale. The bright and grey flake-like intermetallics in the microstructure showed the same elemental distributions as the fine eutectic phases and the needle-like grey phases at position 1, respectively. Phase identification is discussed in the next section.

There was an inconsistency in phase formation between the prediction from the Scheil solidification path in Fig. 5 and the XRD patterns in Fig. 7. The Al_3Ni was not experimentally observed. To study the solidification sequence of the two alloys without Al_3Ni , the Scheil solidification paths for the two alloys were re-calculated with Al_3Ni restricted, as shown in Fig. 9.

The phase $Al_{20}Mn_2Ce$ observed in the experiment was not in the TCAL8 database. This may affect the phase prediction in the Scheil equation. However, the results were still indicative as there are four phases in the calculations with Al_8M_4Ce apparently representing $Al_{20}Mn_2Ce$. In Fig. 9, the freezing ranges of the eutectic reactions in the two alloys were small, 2.8 °C and 3.8 °C, for Alloy A and Alloy B, respectively.

The horizontal expansion and contraction as a function of temperature for the two alloys are shown in Fig. 10. During cooling, the alloys expanded first, followed by contraction. The information extracted from the curves included the linear pre-shrinkage expansion, linear solidification contraction, and linear contraction onset, which was the temperature at which the alloy started to contract. The definitions and the calculation of the linear solidification contraction can be found elsewhere [7,11]. It is the change in linear dimensions of the alloy from the

linear contraction onset to the temperature at the end of solidification (thermal strain accumulated in the solidification range), which determines the hot tearing susceptibility of an alloy.

These properties of Alloy A, Alloy B, and three reference alloys are shown in Table 1. The differences between the linear contraction onset and nonequilibrium solidus (NES) for Alloys A and Alloy B were small, less than 30 $^{\circ}$ C. Compared with three other alloys, the linear preshrinkage expansion of the alloys in this work was larger while their overall linear solidification contraction was one order of magnitude smaller.

The mechanical properties from the Plastometer (PIP) test and tensile test are shown in Table 2. The mechanical properties were obtained by fitting the indentation profile using the constitutive law corresponding to the PIP tests where the material was subject to tensile force in the uniaxial tensile test [43]. The ultimate tensile strength (UTS) of Alloy A and Alloy B at room temperature (RT) was about two and half times larger than their yield strengths, which were 108 MPa and 103 MPa, respectively. The uniform elongation evaluated by the test was above 20 % for the two alloys. For the test at a high temperature (HT), the UTS and elongation retained more than 55 % of the values compared with those properties at RT.

In the tensile tests, the UTS at RT were 137 MPa and 166 MPa for Alloy A and Alloy B, respectively, and dropped at HT to 128 MPa and 137 MPa, respectively. The retention rates for the UTS were 93.4 % and 82.5 % for the two alloys, while the elongation increased with increasing temperature. The RT yield strengths (YS) were 109 MPa and 89 MPa for Alloy A and Alloy B, respectively.

In contrast to UTS and elongation, the YS of each alloy evaluated in different tests was close for the same testing conditions. The YS retention rates for each alloy in the tensile tests and PIP tests, 75% to 74.3% for Alloy A, and 93% to 80% for Alloy B.

The fractography of the two alloys at RT and HT is shown in Fig. 11. The fracture surfaces were perpendicular to the tensile axis. Fractures in the alloys were initiated from the intermetallic phases formed upon solidification reactions at the beginning of solidification (see Figs. 6 and 9). There were limited changes in the fracture surfaces between RT (Fig. 11 a and e, for Alloy A and Alloy B, respectively) and HT (Fig. 11 c and g, for Alloy A and Alloy B, respectively), indicating both alloys

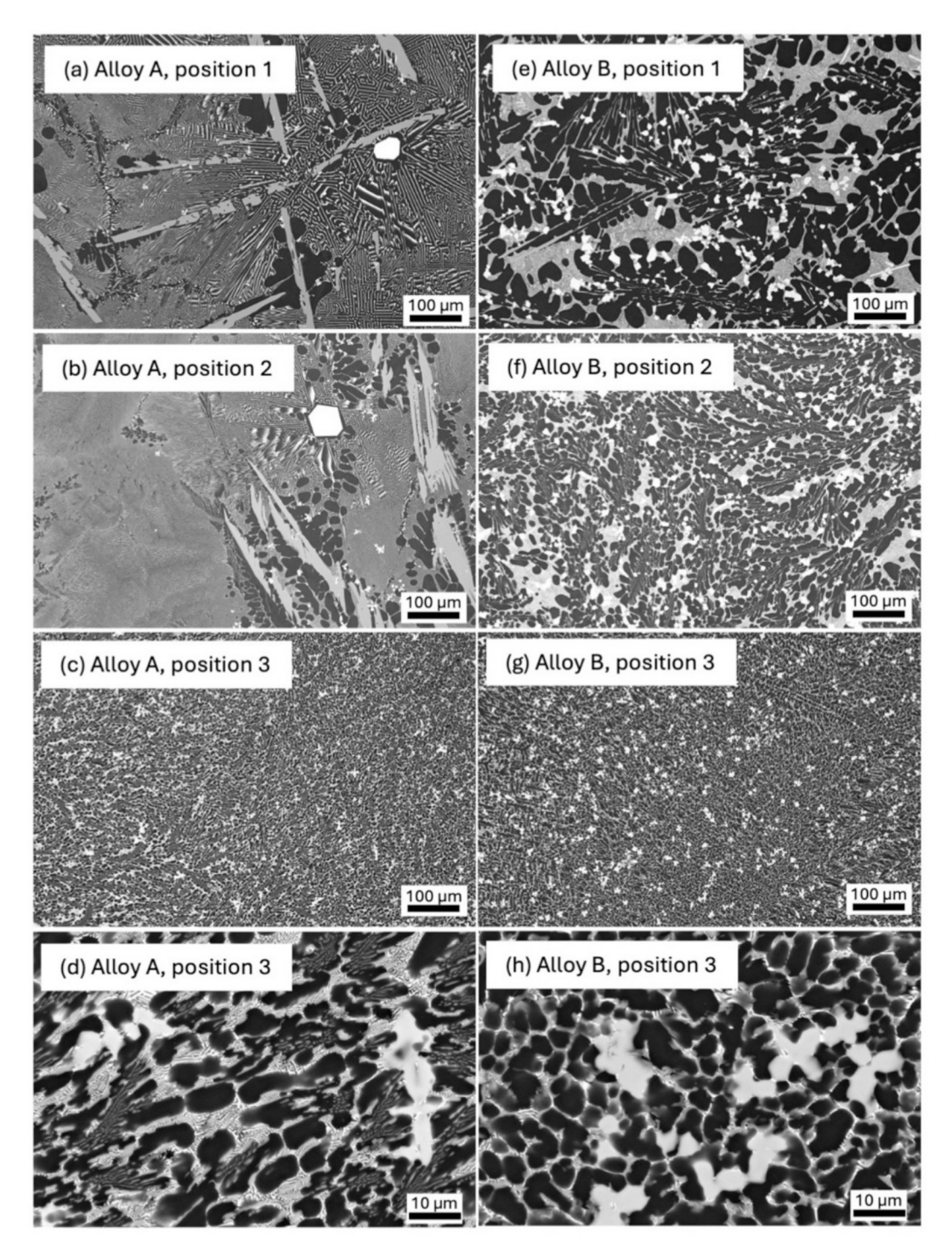


Fig. 6. SEM micrographs (BSE contrast) of Alloy A and Alloy B with different cooling conditions. The positions in the wedge mould are shown in Fig. 1. The cooling speeds were lowest at position 1 (0.33 °C/s) and highest at position 3 (78 °C/s). A higher magnification image for each alloy at position 3 is shown in (d) and (h), respectively.

exhibited thermal stability at elevated temperatures.

Two types of fracture surfaces were observed in both alloys: (1) cleavage planes with flat facets typical of brittle fracture (blue arrows in Fig. 11), and (2) dimples and torn edges typical of ductile fracture located between the cleavage planes (yellow arrows in Fig. 11).

4. Discussion

4.1. Solidification path and solidification contraction in Alloy A and Alloy B

Fig. 10 shows that the alloys expanded at the beginning of the solidification. It was due to the hydrogen dissolved in the melt escaping as the solubility of hydrogen dropped when the temperature decreased, leading to the pre-shrinkage expansion. The expansion depends on composition, melt and solidification conditions [11]. It is noteworthy

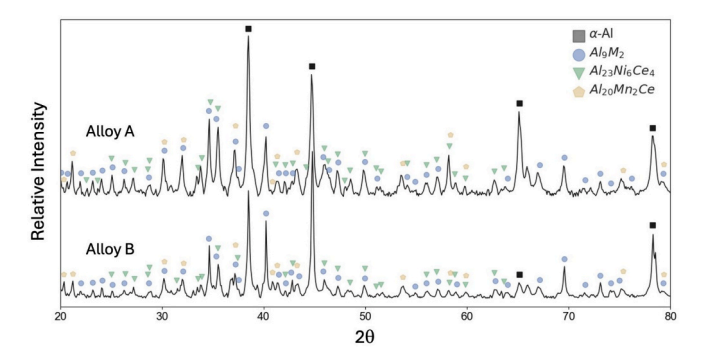


Fig. 7. XRD patterns for Alloy A and Alloy B. The relative intensity shown here was the square root of the measured intensity values in order to reduce the difference in peak heights between Al and other intermetallic phases. M in Al_9M_2 represents Ni and Fe. The PDF numbers for the phase α-Al, Al_9M_2 ($Al_9Ni_{1.3}Fe_{0.7}$), and $Al_{2.3}Ni_6Ce_4$, are 00-004-0787, 01-076-2701, and 01-072-3474, respectively. The crystal structure information of $Al_{20}Mn_2Ce$ was extracted from [41,42].

that the expansion compensated for the overall thermal contraction (thermal strain), reducing further hot tearing susceptibility.

The linear contraction onsets in Alloy A and Alloy B were 649 °C and 662 °C, respectively. They were significantly higher than those in the reference alloys (Table 1). This can be attributed to the compositions with TM and Ce additions. With those additions, the beginning of the solidification and the eutectic reactions in Alloy A and Alloy B occurred at a higher temperature than the reference alloys, where the primary α-Al and intermetallics containing Mg, Cu, Si formed at a lower temperature. While the alloy's thermal stability may benefit from the phases formed at higher temperatures, the parameter critical to the cracking susceptibility is the temperature difference between linear contraction onset and NES, i.e., the vulnerable solidification range. According to Fig. 9, the NES of Alloy A and Alloy B were significantly higher than the solidus of reference alloys. Consequently, the vulnerable solidification ranges in Alloy A and Alloy B were 17.7 °C and 30.4 °C, respectively, significantly smaller than that of the reference alloys (149 $^{\circ}$ C and 77 $^{\circ}$ C for Al-2 Mg and Al-0.4Cu, respectively). The low linear solidification

contraction associated with a small vulnerable solidification range, which indicated good liquid feeding during solidification, demonstrated very small thermal strain accumulated upon solidification and, hence, small hot tearing susceptibility in Alloys A and Alloy B is expected.

The solidification contraction is experimentally measurable only when dendritic networks are formed and strength is developed in the mushy zone, where the material can retain its shape. The linear contraction onset is the temperature at which the alloys start to contract uniformly, as shown in Fig. 10. Generally, the volume fraction of the solid phase corresponding to the linear contraction onset is between 85 % and 95 % in hypoeutectic alloys. In contrast, the volume fractions of solid corresponding to the linear contraction onset in the hypereutectic alloys A and B were 1.79 % and 1.05 %, respectively, as most of the solidification happened within a very narrow temperature range through eutectic reactions. This illustrated a very different contraction development in the tested near-eutectic alloys, making them hot-tearing resistant. Although the hot tearing was not explicitly studied in this work, the unambiguous correlation between the contraction behaviour and hot tearing susceptibility has been established on many occasions before, as in this review [7].

4.2. Phase formation and microstructural evolution at different cooling rates

Both alloys were hypereutectic with intermetallic phase(s) formed first at the beginning of the solidification (Fig. 6 and Fig. 9), respectively. The only difference between the Thermal-calc prediction (Fig. 9) and phase identification in XRD (Fig. 7) was which intermetallic phase containing Mn and Ce was forming, Al_8M_4Ce or $Al_{20}Mn_2Ce$, respectively. Other than this discrepancy, the theoretical calculation was in agreement with the experimental observation: there were three types of intermetallics in the microstructure in addition to the α -Al matrix.

In Alloy A - position 1, where the cooling rate was relatively low (\sim 0.33 °C/s), the grey, plate-like intermetallic (labelled in Fig. S5a) was the only phase exhibiting low contrast of Ce (Fig. 8). Based on the XRD patterns and EDS mapping (Fig. 7 and Fig. 8), this intermetallic was identified as Al₉M₂, see Fig. S3 and Table S3. Given that all three transition metals were detected within the phase, we hypothesise that the

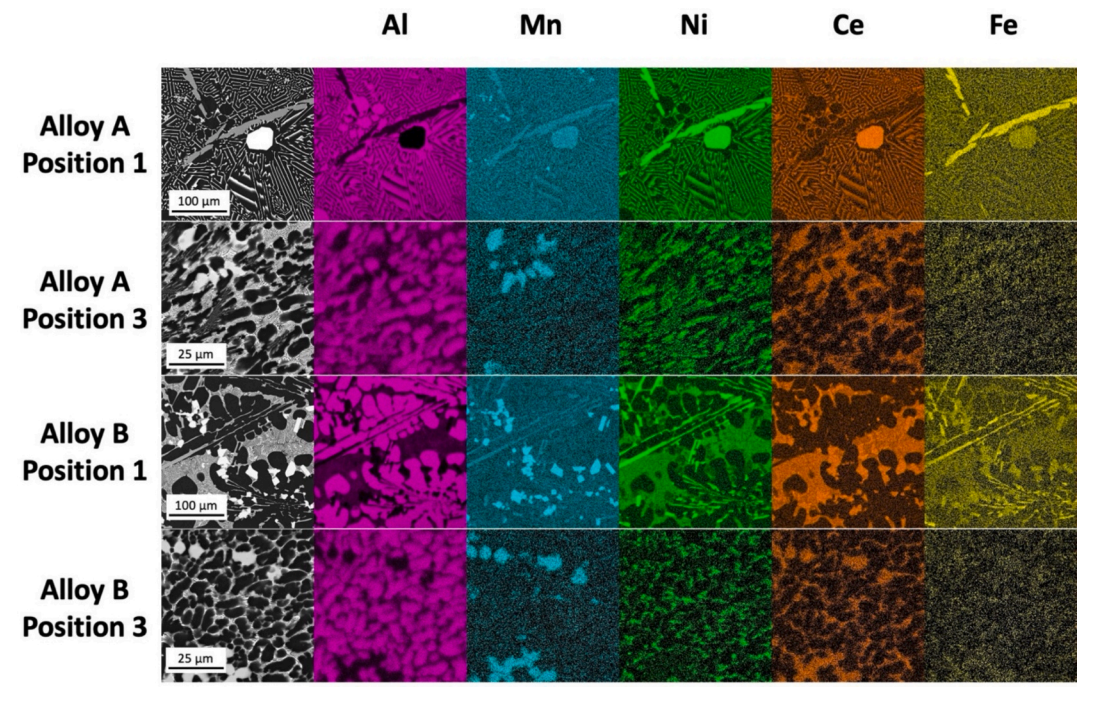


Fig. 8. EDS map analysis showing the elemental distribution of Alloy A and Alloy B at position 1 (slow cooling) and position 3 (fast cooling).

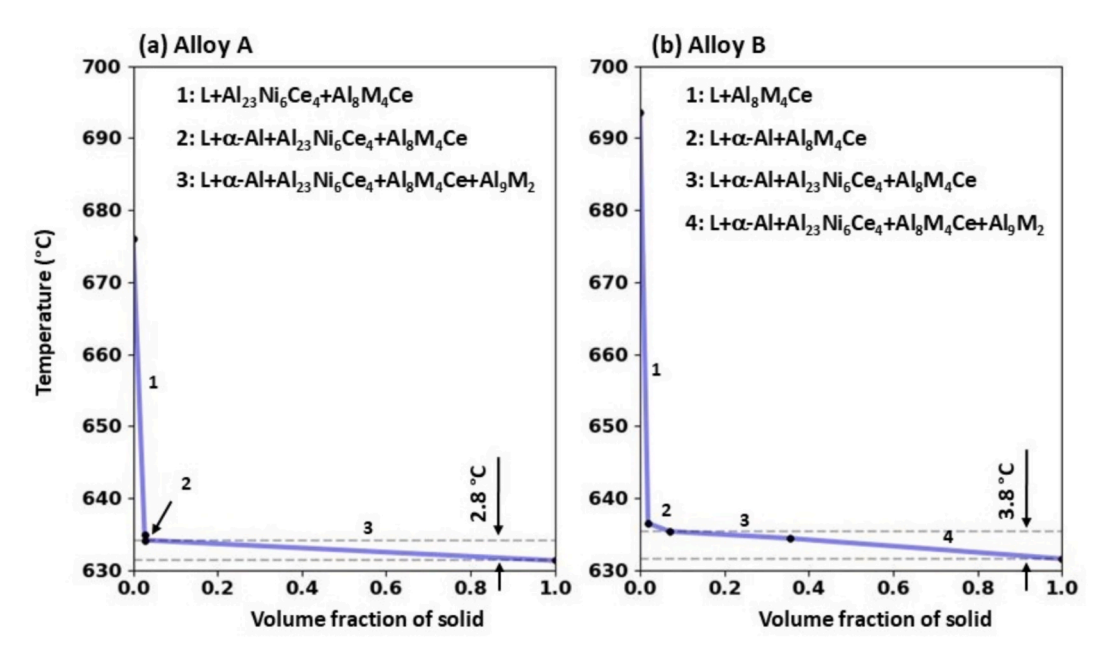


Fig. 9. Solidification paths of (a) Alloy A and (b) Alloy B. The calculations were in the same conditions as those in Fig. 5 with Al₃Ni restricted.

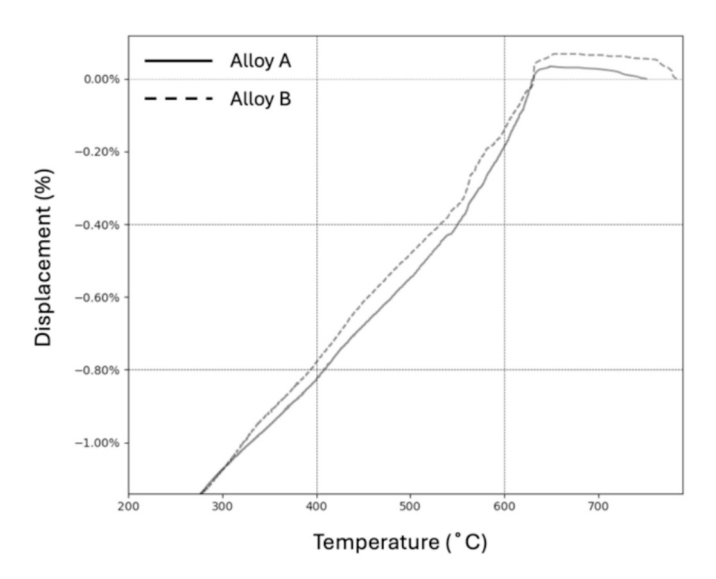


Fig. 10. Horizontal expansion and contraction as a function of temperature for (a) Alloy A and (b) Alloy B.

Table 1 Linear pre-shrinkage expansion ($+ \Delta l$), linear solidification contraction (ε_c), linear contraction onset (t_{co}) and nonequilibrium solidus (NES).

Alloy	$+ \Delta l(\%)$	$\varepsilon_c(\%)$	$t_{co}(^{\circ}C)$	NES	Source
Alloy A	0.066	0.028	649	631.3	This work
Alloy B	0.133	0.025	662	631.6	This work
Al-2 Mg	0.04	0.40	600	451	[11]
6061 Al Alloy	0.02	0.23	599	580	[11]
Al-0.4Cu	_	0.33	638	561	[11]

intermetallic is Al₉(Ni,Fe,Mn)₂. Additionally, EDS point analysis of the bright coarse particle (Fig. 6 and Fig. S5a) revealed a composition of 72.5 at.% Al, 16.2 at.% Ni, 0.5 at.% Fe, 8.4 at.% Ce, and 2.2 at. % Mn. This was consistent with the stoichiometry of Al₂₃Ni₆Ce₄ [33]. The intermetallic phase observed in the eutectic structure appeared to be of the same type as its elemental profile closely resembled that of the

Table 2 Mechanical properties of Alloy A and Alloy B in plastometer test and tensile test. RT: room temperature; HT: high temperature (300 $^{\circ}$ C for 10 min before test); UTS: ultimate tensile strength; YS: yield strength. YS retention is the ratio of the YS at RT to that at HT.

			UTS (MPa)	YS (MPa)	Elongation (%)*	YS retention rate
Plastometer	Alloy A	RT	248 ± 14.5	108 ± 16	21.2 ± 1.6	_
		НТ	142 ±	81 ± 6.5	13.2 ± 0.3	75 %
	Alloy B	RT	263 ± 16.5	103 ± 20	20 ± 0	
		HT	160 ± 7	96 ± 8	14.2 ± 0.8	93 %
Tensile test	Alloy A	RT	$\begin{array}{c} 137\ \pm \\ 16 \end{array}$	$109 \pm \\12$	0.7 ± 0.2	
		HT	$\begin{array}{c} 128 \ \pm \\ 11 \end{array}$	81 ± 3	1.4 ± 0.4	74.3 %
	Alloy B	RT	$\begin{array}{c} 166 \ \pm \\ 21 \end{array}$	89 ± 7	1.6 ± 0.3	
		НТ	$\begin{array}{c} 137 \; \pm \\ 3 \end{array}$	$\begin{array}{c} 71.2 \pm \\ 1.9 \end{array}$	4.8 ± 1.3	80 %

^{*} Elongation in the Plastometer experiment is an estimated value of uniform elongation, see [35] for details.

coarse particle (Fig. 8), this is supported by the Scheil calculation (Fig. 9a). The dispersed fine particles (Fig. S5) were identified as $Al_{20}(Mn,Fe,Ni)_2Ce$, see Fig. S3 and Table S3.

In Alloy B, slow cooling at position 1 in the wedge mould produced a microstructure (Fig. 6e) containing a greater number of dispersed particles. The EDS point analysis showed that they were Al $_{20}$ Mn $_{2}$ Ce (Fig. S4 and Table S4). The eutectic structure consisted of α -Al and Al $_{23}$ (Ni, Fe) $_{6}$ (Ce,Mn) $_{4}$ according to Figs. 7–9. There were also needle-like intermetallics (Fig. S5) between the eutectic colonies. Their chemical compositions were consistent with that of Al $_{9}$ M $_{2}$, as shown in Fig. S4 and Table S4. The Al $_{9}$ M $_{2}$ was finer than the plate-like Al $_{9}$ (Ni,Fe,Mn) $_{2}$ in Alloy A because of the lower Ni concentration in Alloy B.

Microstructures at position 3 were finer due to a higher cooling rate (\sim 78 °C/s). In both alloys, there were two types of eutectic structures: α -Al with the phase of bright contrast and α -Al with the phase of grey contrast. From XRD and EDS analysis (Fig. 7 and Fig. 8), they were

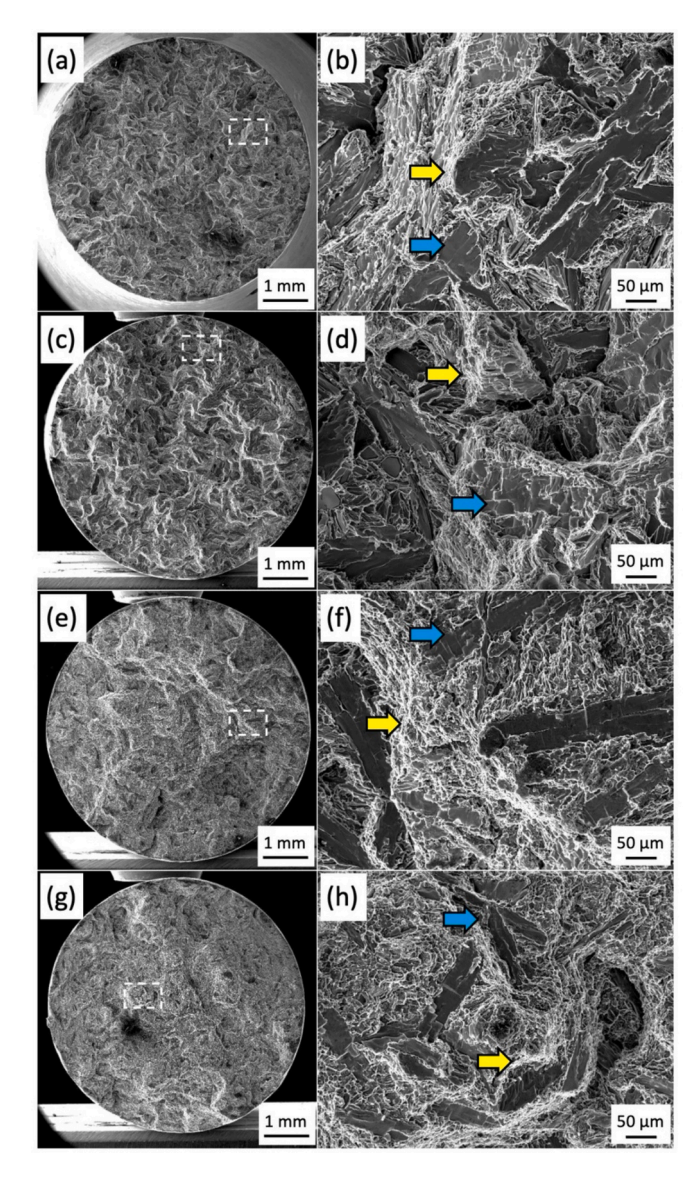


Fig. 11. Fractography of Alloy A and Alloy B at room temperature and high temperature. The fracture surfaces were perpendicular to the tensile axis. (a) and (b) fracture surface of Alloy A at room temperature (c) and (d) fracture surface of Alloy A at high temperature; (e) and (f) fracture surface of Alloy B at room temperature; (g) and (h) fracture surface of Alloy B at high temperature.

identified as $Al_{23}(Ni,Fe)_6(Ce,Mn)_4$ and $Al_9(Ni,Fe,Mn)_2$ for the bright phase and grey phase, respectively. The bright particles distributed in the microstructure were $Al_{20}Mn_2Ce$.

4.3. Mechanical properties at different temperatures

While the YSs obtained from both test methods were similar, there were significant differences in UTS and elongation, as shown in Table 2. In a tensile test, the elongation corresponds to the strain at fracture, whereas fracture characteristics cannot be reliably accessed in a PIP test because the compressive indentation force constrains crack propagation, leading to significantly higher estimated values, which may indicate a defect-lean alloy. The UTS in a tensile test is defined as the maximum stress value in the nominal stress–strain curve, typically corresponding to the onset of necking. While the UTS in the PIP test was also obtained from the nominal stress–strain curve, the curve is actually converted from a true stress-true strain relationship based on the constitutive law, either the Ludwik-Hollomon equation or the Voce equation [43,44]. The two equations are empirical and do not account for the relationship

between the onset of necking and the microstructure, which contributes to the discrepancy in the measured UTS. The YS from PIP and tensile tests were in good agreement for Alloy A, though some differences were observed for Alloy B at both RT and HT. This indicated that the PIP test effectively evaluated the onset of plastic deformation.

From Table 2, Alloy A and B showed significantly higher YS retention rates, compared with the as-cast A319 (below 50 %) [13]. In a typical eutectic structure, the deterioration of strength in Al alloys at high temperature is mainly due to grain/particle coarsening or dissolution of precipitates. Earlier research showed that the constitutive phases in the microstructure, Al₉M₂, Al₂₃(Ni,Fe)₆(Ce,Mn)₄, and Al₂₀Mn₂Ce were thermally stable and resistant to coarsening even at temperatures above 300 °C for hundreds of hours [28,33]. It was attributed to the low solubility and low diffusivity of the alloying elements that prevented the particles from coarsening or dissolution in the matrix. This was further confirmed by the analysis of the fracture surfaces of the two alloys at HT (Fig. 11c and g), as they were similar to those at RT (Fig. 11a and e).

From the fracture morphology in Fig. 11, it seemed the cracking initiated from larger intermetallics by their either brittle facture or separation from the matrix. The presence of cleavage facets (for example, blue arrows in Fig. 11) suggests that brittle fracture modes occur in the two alloys at RT and HT. These flat areas indicate that low-energy fracture paths, along the coarse intermetallics, such as Al_9M_2 and $Al_{20}Mn_2Ce$, were preferred. In contrast, the areas exhibiting dimples and torn edges reflect ductile fracture behaviour. These are eutectic regions consisting of α -Al and $Al_{23}(Ni,Fe)_6(Ce,Mn)_4$, and finely dispersed $Al_{20}Mn_2Ce$ particles.

The combination of the two types of fracture surfaces suggests a mixed-mode fracture mechanism, with localised plasticity interrupting the propagation of brittle cracks. Given the thermal stability of the intermetallics and the strength in the two alloys, the ductility can be improved by modifying the morphology of these phases without significantly compromising the strength at RT and HT.

4.4. Designing alloys with low cracking and high thermal stability

The proposed alloy design methodology is not limited to conventional casting, as demonstrated with Alloys A and B. It can also be used for developing crack resistant alloys for advanced manufacturing processes, such as AM, where rapid cooling rates often lead to high cracking susceptibility in Al alloys. It is concluded that Alloys A and B are highly suitable for AM. Therefore, and as a proof of concept, the two alloys were additively manufactured using a laser directed energy deposition (DED), in a device known as the Blown Powder Additive Manufacturing Process Replicator, 2nd Generation (BAMPRII) [45]. The deposit of Alloy A was free from cracking [46]. Specific conditions of AM, as well as detailed analysis of the structure and phase composition, can be found elsewhere [47]. For illustration, the as-built microstructures in AM and the phases formed are shown in Fig. 12. Compared with the microstructures in Alloy A and Alloy B in the wedge mould, the AM microstructures were much finer due to the higher cooling rate: the largest particles were at scales of micrometres (Fig. 12) instead of tens of micrometres (Fig. 6).

Changes in cooling rate can alter the microstructure's morphology. In the wedge mould, the Al₉(Ni,Fe,Mn)₂, which was plate-like in Alloy A and needle-like in Alloy B (Fig. 6), disappeared and became part of the eutectic structure as the cooling rate increased. It seems that the microstructural morphology of both alloys, being hypereutectic, shifted towards eutectic when the cooling rate increased. It is easy to spot such morphology shift (e.g. from hypereutectic to hypoeutectic) in a binary system, such as Al-Ce [47], when the processing parameters change. For a multi-component system like Alloy A and Alloy B, an understanding of how the morphology shifts toward the eutectic structure with different cooling rates needs further investigation. The predication of the microstructure becomes even more complicated when the cooling rate increases further, such in AM, because metastable phases may form and

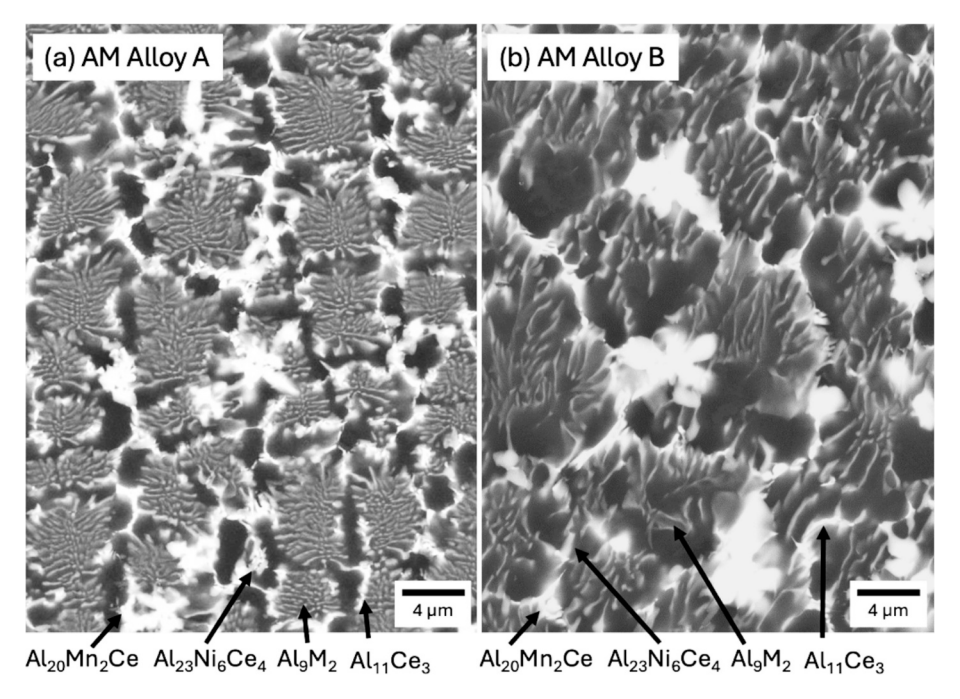


Fig. 12. SEM micrographs (BSE contrast) of Alloy A [46] and Alloy B processed by DED AM. The phases formed in the alloys were labelled. The black areas are the Al matrix.

equilibrium phases may be suppressed. For Alloy A and Alloy B, a new phase, Al₁₁Ce₃, which was not observed in the cast alloys, formed in AM.

The yield strength of AM Alloy A was 70 % higher than that of AlSi10Mg in the same fabrication condition [46]. With alloying elements having low solubility and diffusivity in the Al matrix, the mechanical properties are more stable at elevated temperatures (Table 2), and the yield strength retention rates of both alloys in AM are expected to be higher than AlSi10Mg (commonly used in AM). The experimental results showed that our proposed alloy design method can be applied to various manufacturing methods, including conventional casting and AM.

5. Conclusions

Two new Al alloys containing TMs (Al-4.6Ce-0.3Fe-1.84Mn-5.5Ni and Al-4.6Ce-0.3Fe-2.3Mn-3.84Ni, wt%) were designed using the CAL-PHAD approach, cast in a wedge mould (cooling rates from $0.3~^{\circ}$ C/s to $78~^{\circ}$ C/s) and thoroughly characterised. Their thermal contraction during solidification was measured. Mechanical testing confirmed excellent thermal stability at 300 $^{\circ}$ C for both alloys. This study validates the proposed methodology for designing alloys with enhanced thermal stability and low cracking susceptibility. The main conclusions are shown below:

- 1. Two compositions of Al alloys with a low freezing range, $2.8\,^{\circ}$ C/s and $3.8\,^{\circ}$ C/s for Alloy A and Alloy B, respectively. Both showed low solidification contraction, an order of magnitude lower than that of an AA6061 Al alloy indicating low hot cracking susceptibility.
- 2. Microstructural analysis revealed three types of constitutive particles: Al_9M_2 , $Al_{23}(Ni,Fe)_6(Ce,Mn)_4$, and $Al_{20}Mn_2Ce$. Phases predicted by Thermo-calc, such as Al_8M_4Ce and Al_3Ni , were not observed upon solidification across the tested cooling rates.
- 3. Mechanical properties were evaluated using PIP and tensile testing with consistent YS values. Both alloys retained over 74 % of their YS at 300 °C, exhibited excellent thermal stability attributed to the coarsening-resistant phases in the microstructure.

The testing and characterisation results confirmed the effectiveness of the proposed methodology for designing thermally stable and crack-free Al alloys suitable for AM.

CRediT authorship contribution statement

Chengbo Zhu: Writing – review & editing, Writing – original draft, Formal analysis, Data curation, Conceptualization. Da Guo: Formal analysis, Data curation. Chu Lun Alex Leung: Writing – review & editing, Supervision, Funding acquisition. Iakovos Tzanakis: Writing – review & editing, Supervision, Funding acquisition. Peter D. Lee: Writing – review & editing, Supervision, Funding acquisition. Dmitry Eskin: Writing – review & editing, Supervision, Methodology, Funding acquisition, Formal analysis, Conceptualization.

Declaration of competing interest

The authors declare that they have no known competing financial interests or personal relationships that could have appeared to influence the work reported in this paper.

Acknowledgement

The research for this work was made possible through funding from the UK Engineering and Physical Sciences Research Council (EPSRC) via the Performance-driven design of aluminium alloys for additive manufacturing (PAAM) project, which is granted under the following numbers: EP/W00593X/1, EP/W006774/1, EP/W006154/1. The authors also acknowledge the scientific and technical assistance of the Experimental Techniques Centre (ETC) at Brunel University London. CLAL is funded by IPG Photonics/ Royal Academy of Engineering Senior Research Fellowship in SEARCH (ref: RCSRF2324-18-71). PDL is funded by support from a Royal Academy of Engineering Chair in Emerging Technologies [grant number CiET1819/10]. This work was also supported by other EPSRC-funded projects, including EP/W037483/1, EP/W003333/1, and EP/V061798/1.

Appendix A. Supplementary data

Supplementary data to this article can be found online at https://doi.org/10.1016/j.matdes.2025.115152.

Data availability

Original data can be made available upon request to the corresponding author.

References

- J.P. Immarigeon, et al., Lightweight materials for aircraft applications, Mater. Charact. 35 (1) (1995) 41–67.
- [2] I.N. Fridlyander, et al., Aluminum Alloys: Promising Materials in the Automotive Industry, Met. Sci. Heat Treat. 44 (9) (2002) 365–370.
- [3] W. Zhang, J. Xu, Advanced lightweight materials for automobiles: a review, Mater. Des. 221 (2022) 110994.
- [4] L. Arnberg, et al., Solidification Characteristics of Aluminum Alloys: Dendrite Coherency, American Foundreymen's Society, 1996.
- [5] D.G. Eskin, L. Katgerman, A quest for a new hot tearing criterion, Metall. Mater. Trans. A 38 (7) (2007) 1511–1519.
- [6] T. Magnusson, L. Arnberg, Density and solidification shrinkage of hypoeutectic aluminum-silicon alloys, Metall. Mater. Trans. A 32 (10) (2001) 2605–2613.
- [7] D.G. Eskin, Suyitno, L. Katgerman, Mechanical properties in the semi-solid state and hot tearing of aluminium alloys, Prog. Mater Sci. 49 (5) (2004) 629–711.
- [8] L. Sweet, et al., Hot tear susceptibility of Al-Mg-Si-Fe alloys with varying iron contents, Metall. Mater. Trans. A 44 (12) (2013) 5396–5407.
- [9] S. Vernède, P. Jarry, M. Rappaz, A granular model of equiaxed mushy zones: Formation of a coherent solid and localization of feeding, Acta Mater. 54 (15) (2006) 4023–4034.
- [10] D. Eskine, J. Zuidema Jr, L. Katgerman, Linear solidification contraction of binary and commercial aluminium alloys, Int. J. Cast Met. Res. 14 (4) (2002) 217–223.
- [11] D.G. Eskin, et al., Contraction of aluminum alloys during and after solidification, Metall. Mater. Trans. A 35 (4) (2004) 1325–1335.
- [12] Q.G. Wang, Microstructural effects on the tensile and fracture behavior of aluminum casting alloys A356/357, Metall. Mater. Trans. A 34 (12) (2003) 2887–2899.
- [13] E. Rincon, et al., Temperature effects on the tensile properties of cast and heat treated aluminum alloy A319, Mater. Sci. Eng. A 519 (1) (2009) 128–140.
- [14] I.M. Lifshitz, V.V. Slyozov, The kinetics of precipitation from supersaturated solid solutions, J. Phys. Chem. Solid 19 (1) (1961) 35–50.
- [15] F. Czerwinski, Thermal stability of aluminum alloys, Materials 13 (2020) 15.
- [16] F. Czerwinski, Cerium in aluminum alloys, J. Mater. Sci. 55 (1) (2020) 24-72.
- [17] Z.C. Sims, et al., Cerium-based, intermetallic-strengthened aluminum casting alloy: high-volume co-product development, JOM 68 (7) (2016) 1940–1947.
- [18] F. Czerwinski, Thermal stability of aluminum-cerium binary alloys containing the Al-Al11Ce3 eutectic, Mater. Sci. Eng. A 809 (2021) 140973.
- [19] S.-I. Fujikawa, K.-I. Hirano, Y. Fukushima, Diffusion of silicon in aluminum, Metall. Trans. A 9 (12) (1978) 1811–1815.
- [20] K.E. Knipling, D.C. Dunand, and N. Seidman, Criteria for developing castable, creep-resistant aluminum-based alloys – A review. 97(3) (2006) 246–265.
- [21] D. Weiss, Improved high-temperature aluminum alloys containing cerium, J. Mater. Eng. Perform. 28 (4) (2019) 1903–1908.
- [22] S. Keerti, et al., High-temperature mechanical behaviour of Al-10Ce alloy with Sc, Zr, Si, and Mg alloying elements, Mater. Des. 248 (2024) 113524.
- [23] D.R. Manca, et al., Microstructure and properties of novel heat resistant Al-Ce-Cu alloy for additive manufacturing, Met. Mater. Int. 25 (3) (2019) 633-640.

- [24] A.V. Krainikov, O.D. Neikov, Rapidly solidified high-temperature aluminum alloys. II. Mechanical properties, Powder Metall. Met. Ceram. 51 (9) (2013) 554–565.
- [25] N.A. Belov, E.A. Naumova, D.G. Eskin, Casting alloys of the Al-Ce-Ni system: microstructural approach to alloy design, Mater. Sci. Eng. A 271 (1) (1999) 134-142
- [26] T. Wu, et al., Microstructure and creep properties of cast near-eutectic Al-Ce-Ni alloys, Mater. Sci. Eng. A 833 (2022) 142551.
- [27] F. Schurack, J. Eckert, L. Schultz, Synthesis and mechanical properties of cast quasicrystal-reinforced Al-alloys, Acta Mater. 49 (8) (2001) 1351–1361.
- [28] A. Plotkowski, et al., Microstructure and properties of a high temperature Al-Ce-Mn alloy produced by additive manufacturing, Acta Mater. 196 (2020) 595-608
- [29] J. Kozakevich, et al., Interplay between cooling rate, microstructure, and mechanical properties of an Al–Ce–Ni–Mn alloy. Light Metals 2022, Springer International Publishing, Cham, 2022.
- [30] T. Wu, et al., Microstructure and mechanical properties of hypoeutectic Al-6Ce-3Ni-0.7Fe (wt.%) alloy, Mater. Sci. Eng. A 875 (2023) 145072.
- [31] R.A. Michi, et al., Additively manufactured Al-Ce-Ni-Mn alloy with improved elevated-temperature fatigue resistance, Addit. Manuf. 66 (2023) 103477.
- [32] C.N. Ekaputra, J.-E. Mogonye, D.C. Dunand, Microstructure and mechanical properties of cast, eutectic Al-Ce-Ni-Mn-Sc-Zr alloys with multiple strengthening mechanisms, Acta Mater. 274 (2024) 120006.
- [33] C.N. Ekaputra, et al., Design and characterization of hierarchically-strengthened, cast Al-Ce-Ni-Mn-Sc-Zr alloys for high-temperature applications. Light Metals 2024, Springer Nature, Switzerland, 2024.
- [34] J.O. Andersson, et al., Thermo-Calc & DICTRA, computational tools for materials science, Calphad 26 (2) (2002) 273–312.
- [35] W. Gu, et al., Indentation plastometry of welds, Adv. Eng. Mater. 24 (9) (2022) 2101645.
- [36] A. International, ASTM Standard E8/E8M- 24, Standard Test Methods for Tension Testing of Metallic Materials, West Conshohocken, PA, United States, 2024.
- [37] S. Chankitmunkong, D.G. Eskin, C. Limmaneevichitr, Structure refinement, mechanical properties and feasibility of deformation of hypereutectic Al–Fe–Zr and Al–Ni–Zr alloys subjected to ultrasonic melt processing, Mater. Sci. Eng. A 788 (2020) 139567.
- [38] A.E. Perrin, et al., Effect of Mn on eutectic phase equilibria in Al-rich Al-Ce-Ni alloys, J. Alloy. Compd. 965 (2023) 171455.
- [39] S. Bahl, et al., An additively manufactured near-eutectic Al-Ce-Ni-Mn-Zr alloy with high creep resistance, Acta Mater. 268 (2024) 119787.
- [40] X. Wang, et al., Mechanistic understanding on the evolution of nanosized Al3Fe phase in Al-Fe alloy during heat treatment and its effect on mechanical properties, Mater. Sci. Eng. A 751 (2019) 23–34.
- [41] S. Samson, The crystal structure of the intermetallic compound Mg/sb 3Cr/sb 2Al/sb 18, Acta Crystallogr. 11 (12) (1958) 851–857.
- [42] M.A. Gordillo, et al., Phase stability in a powder-processed Al-Mn-Ce alloy, J. Mater. Sci. 49 (10) (2014) 3742–3754.
- [43] J.E. Campbell, et al., Comparison between stress-strain plots obtained from indentation plastometry, based on residual indent profiles, and from uniaxial testing, Acta Mater. 168 (2019) 87–99.
- [44] J.E. Campbell, et al., Experimental and computational issues for automated extraction of plasticity parameters from spherical indentation, Mech. Mater. 124 (2018) 118–131.
- [45] C.L.A. Leung, et al., In situ X-ray imaging of defect and molten pool dynamics in laser additive manufacturing, Nat. Commun. 9 (1) (2018) 1355.
- [46] D. Guo, et al., Mechanical and in-situ thermal behavior upon directed energy deposition additive manufacturing of a new high-performance Al alloy. Int. J. Extreme Manufact. (2025). Accepted.
- [47] A. Plotkowski, et al., Evaluation of an Al-Ce alloy for laser additive manufacturing, Acta Mater. 126 (2017) 507–519.